Performance of the electronic readout of the ATLAS liquid argon calorimeters

2010 JINST 5 P09003

(http://iopscience.iop.org/1748-0221/5/09/P09003)

Jinst

PUBLISHED BY IOP PUBLISHING FOR SISSA

RECEIVED: *May 5, 2010*
ACCEPTED: *June 30, 2010*
PUBLISHED: *September 7, 2010*

Performance of the electronic readout of the ATLAS liquid argon calorimeters

H. Abreu,[t] M. Aharrouche,[n] M. Aleksa,[f] L. Aperio-Bella,[b] J.P. Archambault,[e] S. Arfaoui,[f,o] O. Arnaez,[b] E. Auge,[t] M. Aurousseau,[b] S. Bahinipati,[a] J. Ban,[x,g] D. Banfi,[p,q] A. Barajas,[r] T. Barillari,[r] A. Bazan,[b] F. Bellachia,[b] O. Beloborodova,[s] D. Benchekroun,[v] K. Benslama,[u] N. Berger,[b] F. Berghaus,[ac] P. Bernat,[t] R. Bernier,[t] N. Besson,[w] S. Binet,[t] J.B. Blanchard,[t] A. Blondel,[j] V. Bobrovnikov,[s] O. Bohner,[t] M. Boonekamp,[w] S. Bordoni,[m] M. Bouchel,[t] C. Bourdarios,[t] A. Bozzone,[t] H.M. Braun,[ad] D. Breton,[t] H. Brettel,[r] G. Brooijmans,[g] R. Caputo,[y] T. Carli,[f] L. Carminati,[p,q] S. Caughron,[g] P. Cavalleri,[m] D. Cavalli,[p] E. Chareyre,[m] R.L. Chase,[t] S.V. Chekulaev,[ab] H. Chen,[d] A. Cheplakov,[l] R. Chiche,[t] M. Citterio,[p] C. Cojocaru,[e] J. Colas,[b] C. Collard,[t] J. Collot,[k] M. Consonni,[b] M. Cooke,[g] K. Copic,[g,1] G.C. Costa,[p] L. Courneyea,[ac] D. Cuisy,[t] W.D. Cwienk,[r] D. Damazio,[d] D. Dannheim,[f,r] S. De Cecco,[m] X. De la Broise,[w] C. De La Taille,[t] J.B. De Vivie,[t] B. Debennerot,[t] E. Delagnes,[w] M. Delmastro,[f] F. Derue,[m] S. Dhaliwal,[aa] L. Di Ciaccio,[b] O. Doan,[b] F. Dudziak,[t] L. Duflot,[t] N. Dumont-Dayot,[b] D. Dzahini,[k] S. Elles,[b] E. Ertel,[n] M. Escalier,[t] A.I. Etienvre,[w] I. Falleau,[t] M. Fanti,[p,q] T. Farooque,[aa] P. Favre,[t] Lo. Fayard,[t] J. Fent,[r] J. Ferencei,[x] A. Fischer,[r] D. Fournier,[t] L. Fournier,[b] M. Fras,[r] R. Froeschl,[f] T. Gadfort,[d] M.L. Gallin Martel,[k] A. Gibson,[aa] D. Gillberg,[e] D.M. Gingrich,[a] T. Goepfert,[i] J. Goodson,[y] M. Gouighri,[v] C. Goy,[b] V. Grassi,[p] J. Gray,[y] T. Guillemin,[b] B. Guo,[aa] J. Habring,[r] C. Handel,[n] L. Heelan,[e] H. Heintz,[r] L. Helary,[b] S. Henrot-Versille,[t] L. Hervas,[f] J. Hobbs,[y] J. Hoffman,[h] J.Y. Hostachy,[k] A. Hoummada,[v] J. Hrivnac,[t] T. Hrynova,[b] F. Hubaut,[o] J. Huber,[r] L. Iconomidou-Fayard,[t] P. Iengo,[b] P. Imbert,[t] R. Ishmukhametov,[h] A. Jantsch,[r] N. Javadov,[l] S. Jézéquel,[b] M. Jimenez Belenguer,[f] X.Y Ju,[u] M. Kado,[t] A. Kalinowski,[u] D. Kar,[u] A. Karev,[r] I. Katsanos,[g] M. Kazarinov,[l] N. Kerschen,[f] J. Kierstead,[d] M.S. Kim,[a] A. Kiryunin,[r] E. Kladiva,[x] N. Knecht,[aa] M. Kobel,[i] I. Koletsou,[b] S. König,[n] P. Krieger,[aa] V. Kukhtin,[l] M. Kuna,[o] L. Kurchaninov,[r,ab] J. Labbé,[b,k] D. Lacour,[m] E. Ladygin,[l] R. Lafaye,[b] B. Laforge,[m] D. Lamarra,[j]

[1]Corresponding author.

doi:10.1088/1748-0221/5/09/P09003

2010 JINST 5 P09003

W. Lampl,[c] F. Lanni,[d] S. Laplace,[b] H. Laskus,[r] A. Le Coguie,[w] O. Le Dortz,[m] C. Le Maner,[aa] M. Lechowski,[t] S.C. Lee,[z] M. Lefebvre,[ac] K. Leonhardt,[i] L. Lethiec,[t] J. Leveque,[o] Z. Liang,[z] Ch. Liu,[e] T. Liu,[h] Y. Liu,[o] P. Loch,[c] J. Lu,[a] H. Ma,[d] W. Mader,[i] S. Majewski,[d] N. Makovec,[t] D. Makowiecki,[d] L. Mandelli,[p] P.S. Mangeard,[o] B. Mansoulié,[w] J.F. Marchand,[b] G. Marchiori,[m] D. Martin,[m] G. Martin-Chassard,[t] B. Martin dit Latour,[j] A. Marzin,[w] A. Maslennikov,[s] N. Massol,[b] P. Matricon,[t] D. Maximov,[s] M. Mazzanti,[p] T. McCarthy,[y] R. McPherson,[ac] S. Menke,[r] J.P. Meyer,[w] Y. Ming,[u] E. Monnier,[o] P. Mooshofer,[r] A. Neganov,[l] F. Niedercorn,[t] I. Nikolic-Audit,[m] I.M. Nugent,[ab] G. Oakham,[e] H. Oberlack,[r] J. Ocariz,[m] J. Odier,[o] C.J. Oram,[ab] I. Orlov,[s] R. Orr,[aa] J.A. Parsons,[g] S. Peleganchuk,[s] A. Penson,[g] L. Perini,[p,q] P. Perrodo,[b] G. Perrot,[b] A. Perus,[t] E. Petit,[o] I. Pisarev,[l] M. Plamondon,[ac] P. Poffenberger,[ac] L. Poggioli,[t] G. Pospelov,[r] P. Pralavorio,[o] J. Prast,[b] X. Prudent,[i] H. Przysiezniak,[b] P. Puzo,[t] M. Quentin,[t] V. Radeka,[d] S. Rajagopalan,[d] E. Rauter,[r] O. Reimann,[r] S. Rescia,[d] B. Resende,[o] J.P. Richer,[t,k] M. Ridel,[m] R. Rios,[h] L. Roos,[m] G. Rosenbaum,[aa] H. Rosenzweig,[t] O. Rossetto,[k] W. Roudil,[t] D. Rousseau,[t] X. Ruan,[t] A. Rudert,[r] N. Rusakovich,[l] P. Rusquart,[t] J. Rutherfoord,[c] G. Sauvage,[b] A. Savine,[c] J. Schaarschmidt,[i] P. Schacht,[r] A. Schaffer,[t] M. Schram,[e] P. Schwemling,[m] N. Seguin Moreau,[t] F. Seifert,[i] L. Serin,[t] R. Seuster,[r,ac] A. Shalyugin,[l] M. Shupe,[c] S. Simion,[t] P. Sinervo,[aa] W. Sippach,[g] K. Skovpen,[s] R. Sliwa,[t] A. Soukharev,[s] F. Spano,[g] P. Stavina,[x] A. Straessner,[i] P. Strizenec,[x] R. Stroynowski,[h] A. Talyshev,[s] S. Tapprogge,[n] F. Tarrade,[d] G.F. Tartarelli,[p] R. Teuscher,[aa] Yu. Tikhonov,[s] V. Tocut,[t] D. Tompkins,[c] P. Thompson,[aa] S. Tisserant,[o] T. Todorov,[b] F. Tomasz,[x] S. Trincaz-Duvoid,[m] N. Trinh Thi,[m] S. Trochet,[t] B. Trocmé,[k] K. Tschann-Grimm,[y] D. Tsionou,[b] R. Ueno,[e] G. Unal,[f] D. Urbaniec,[g] Y. Usov,[l] K. Voss,[ac] J.J. Veillet,[t] M. Vincter,[e] S. Vogt,[r] Z. Weng,[z] K. Whalen,[e] F. Wicek,[t] H. Wilkens,[f] I. Wingerter-Seez,[b] E. Wulf,[g] Z. Yang,[e] J. Ye,[h] L. Yuan,[m] A. Yurkewicz,[y] P. Zarzhitsky,[h] D. Zerwas,[t] H. Zhang,[o] L. Zhang,[g] N. Zhou,[g] J. Zimmer,[r] R. Zitoun[b] and L. Zivkovic[g]

[a] *University of Alberta, Department of Physics, Centre for Particle Physics, Edmonton, AB T6G 2G7, Canada*

[b] *LAPP, Université de Savoie, CNTS/IN2P3, Annecy-le-Vieux, France*

[c] *University of Arizona, Department of Physics, Tucson, AZ 85721, United States of America*

[d] *Brookhaven National Laboratory, Physics Department, Bldg. 510A, Upton, NY 11973, United States of America*

[e] *Carleton University, Department of Physics, 1125 Colonel By Drive, Ottawa ON K1S 5B6, Canada*

[f] *CERN, CH 1211 Geneva 23, Switzerland*

[g] *Columbia University, Nevis Laboratory, 136 So. Broadway, Irvington, NY 10533, United States of America*

[h] *Southern Methodist University, Physics Department, 106 Fondren Science Building, Dallas, TX 75275-0175, United States of America*

[i] *Technical University Dresden, Institut fuer Kern- und Teilchenphysik, Zellescher Weg 19, D-01069 Dresden, Germany*

[j] *Université de Genève, section de Physique, 24 rue Ernest Ansermet, CH-1211 Geneva 4, Switzerland*

2010 JINST 5 P09003

[k] *Laboratoire de Physique Subatomique et de Cosmologie, CNRS/IN2P3, Université Joseph Fourier, INPG, 53 avenue des Martyrs, FR 38026 Grenoble Cedex, France*
[l] *Joint Institute for Nuclear Research, JINR Dubna, RU 141 980Moscow Region, Russia*
[m] *Laboratoire de Physique Nucléaire et de Hautes Energies, Université Pierre et Marie Curie (Paris 6), Université Denis Diderot (Paris 7), CNRS/IN2P3, Tour 33, 4 place Jussieu, FR 75252 Paris Cedex 05, France*
[n] *Universitaet Mainz, Institut fuer Physik, Staudinger Weg 7, DE 55099 Mainz, Germany*
[o] *CPPM, Aix-Marseille Université, CNRS/IN2P3, Marseille, France*
[p] *INFN Sezione di Milano, via Celoria 16, IT - 20133 Milano, Italy*
[q] *Università di Milano, Dipartimento di Fisica, via Celoria 16, IT-20133 Milano, Italy*
[r] *Max-Planck-Institut für Physik, (Werner-Heisenberg-Institut), Föhringer Ring 6, 80805 München, Germany*
[s] *Budker Institute of Nuclear Physics (BINP), RU Novosibirsk 630 090, Russia*
[t] *LAL, Université Paris-Sud, IN2P3/CNRS, Orsay, France*
[u] *University of Regina, Physics Department, Canada*
[v] *Université Hassan II, Faculté des Sciences Ain Chock, B.P. 5366, MA - Casablanca*
[w] *CEA, DSM/IRFU, Centre d'Etudes de Saclay, FR 91191 Gif-sur-Yvette, France*
[x] *Comenius University, Faculty of Mathematics, Physics & Informatics, Mlynska dolina F2, SK 84258 Bratislava, Institute of Experimental Physics of the Slovak Academy of Sciences, Dept. of Subnuclear Physics, Watsonova 47, SK 04353 Kosice, Slovak Republic*
[y] *Stony Brook University, Department of Physics and Astronomy, Nicolls Road, Stony Brook, NY 11794-3800, United States of America*
[z] *Insitute of Physics, Academia Sinica, TW-Taipei 11529, Taiwan*
[aa] *University of Toronto, Department of Physics, 60 Saint George Street, Toronto M5S 1A7, Ontario, Canada*
[ab] *TRIUMF, 4004 Wesbrook Mall, Vancouver, B.C. V6T 2A3, Canada*
[ac] *University of Victoria, Department of Physics and Astronomy, P.O. Box 3055, Victoria B.C., V8W 3P6, Canada*
[ad] *Bergische Universitat, Fachbereich C, Physik, Postfach 100127, Gauss-Strasse 20, D- 42097 Wuppertal, Germany*

E-mail: kcopic@nevis.columbia.edu

ABSTRACT: The ATLAS detector has been designed for operation at the Large Hadron Collider at CERN. ATLAS includes electromagnetic and hadronic liquid argon calorimeters, with almost 200,000 channels of data that must be sampled at the LHC bunch crossing frequency of 40 MHz. The calorimeter electronics calibration and readout are performed by custom electronics developed specifically for these purposes. This paper describes the system performance of the ATLAS liquid argon calibration and readout electronics, including noise, energy and time resolution, and long term stability, with data taken mainly from full-system calibration runs performed after installation of the system in the ATLAS detector hall at CERN.

KEYWORDS: Digital signal processing (DSP); Electronic detector readout concepts (gas, liquid); Calorimeters; Front-end electronics for detector readout

2010 JINST 5 P09003

Contents

1 Introduction **1**

2 Overview of the ATLAS LAr readout electronics **2**

3 Pulse reconstruction and calibration **5**

4 Pedestal and noise performance **9**
- 4.1 Electronic noise 10
- 4.2 System isolation and noise performance 11
- 4.3 Coherent noise 12
- 4.4 Pedestal and noise stability 12

5 Energy measurement **14**
- 5.1 Energy resolution of the electromagnetic calorimeter 15
- 5.2 Linearity 16
- 5.3 Stability of the energy measurement 16
- 5.4 Crosstalk 17

6 Time measurement **17**
- 6.1 Time resolution 18
- 6.2 Time uniformity 20

7 Performance of the Back End electronics **20**
- 7.1 Digital signal processing 20
- 7.2 Processing time 23

8 Summary **23**

2010 JINST 5 P09003

1 Introduction

ATLAS [1] is a large general-purpose particle detector designed for operation at the Large Hadron Collider (LHC) [2] at CERN. The LHC will create proton-proton collisions with a center-of-mass energy up to 14 TeV. The ATLAS detector is made up of several concentric systems designed to measure the properties of particles created in these collisions. Closest to the collision point, semiconductor and transition radiation trackers measure the interactions of charged particles as they pass through ATLAS. The trackers are contained inside of a 2 T solenoid, which provides charge identification for the particles. Outside of the solenoid, liquid argon (LAr) and tile calorimeters measure the energy of particle showers. Farthest from the collision point, a muon spectrometer with an air-core toroid system detects muons which pass through the rest of the detector.

The LAr calorimeters are sampling calorimeters with LAr used as the active medium. There are several subdetectors inside three separate cryostats. The electromagnetic barrel (EMB) calorimeter, inside its own cryostat, provides coverage in the central region of the detector. Two endcap (EC) cryostats each contain an electromagnetic endcap (EMEC) calorimeter, a hadronic endcap (HEC) calorimeter, and a forward calorimeter (FCal). Each detector is segmented such that particles traveling from the collision point encounter towers in the $\eta - \phi$ plane.[1] For the electromagnetic (EM) calorimeters, these towers are projective. In addition to this transverse segmentation, the calorimeters are also divided into layers in depth. In the region $|\eta| < 1.8$, particles first encounter an instrumented argon layer called the presampler (PS). The PS measurement is used to estimate energy lost upstream in this region, where at least two radiation lengths of material are present. There are two to three EM layers in the EMB or EMEC, depending on the η position. Behind the EMEC, the HEC has four layers in depth. The FCal has three layers, reaching the highest η of 4.9. The detector capacitance over the various subsystems ranges from 20 pF to 3 nF, with the EMB ranging from $\sim$200 pF to 2 nF, for example. More details about the design, construction, and performance of the calorimeters themselves can be found in reference [1] and the references contained therein. The state of the system at the start of the LHC running is described in reference [3].

The LAr calorimeters are read out via a system of custom electronics. Wherever possible, the same front end and back end electronics are used for the different subdetectors. Previous papers [4–7] have described in detail the overall system architecture as well as the design and implementation of individual components of the LAr readout. The purpose of this paper is to describe the full system performance of these custom electronics. Often, a result for only one subdetector is shown, but as the electronics are identical unless otherwise stated, the result will hold for all the LAr systems. The measured performance of the precision readout of the individual calorimeter channels is presented, including some results from dedicated tests but focusing on analyses of calibration data taken during the commissioning of the entire system, as it is now installed in the ATLAS cavern at CERN.

This paper is organized as follows: section 2 provides a brief overview of the LAr readout electronics, followed in section 3 by a description of the methods used to reconstruct the calorimeter pulses. System performance results are then presented, with section 4 discussing the pedestal and noise performance, section 5 the energy reconstruction including linearity and resolution, section 6 the timing performance, and section 7 the performance of the Back End electronics. A brief summary then follows in section 8.

2 Overview of the ATLAS LAr readout electronics

The electronic readout of the ATLAS LAr calorimeters, depicted schematically in figure 1, is divided into a Front End (FE) system [4] of circuit boards mounted in custom crates directly on the detector cryostats, and a Back End (BE) system [5] of VME-based boards located off the detector, outside the detector hall. The FE system includes Front End Boards (FEBs) [6], which perform the readout and digitization of the calorimeter signals, calibration boards [7] which inject precision calibration signals, layer sum boards which produce analog sums for the Level 1 (L1) trigger system,

[1] In the ATLAS coordinate system, ϕ is the azimuthal angle around the axis of the beam; θ is the polar angle from the beam axis. The pseudorapidity, η, is defined as $\eta = -\ln\tan(\theta/2)$.

2010 JINST 5 P09003

and control boards which receive and distribute the 40 MHz LHC clock as well as other configuration and control signals. The BE electronics are made up primarily of Read Out Driver (ROD) boards which receive the digitized signals from the FEBs over 1.6 Gbps optical links. The RODs perform digital filtering, formatting, and monitoring of the calorimeter signals before transmitting the processed data to the ATLAS data acquisition system (DAQ).

The LAr readout was designed to meet demanding specifications. The ATLAS LAr calorimeters are finely segmented, with a total of 182,468 channels to be read out. With each FEB handling up to 128 channels, a total of 1524 FEBs are required, distributed among 58 FE crates mounted on the various cryostats. All of the on-detector FE electronics have been built to withstand the high levels of radiation [8, 9] which result from the collisions of the intense LHC beams. The FEBs sample the LAr calorimeter signals at the LHC bunch crossing frequency of 40 MHz and store the samples during the latency of the ATLAS L1 trigger system. For an initial maximum L1 trigger rate of 75 kHz (increasing later to 100 kHz), the FEB reads out five samples per channel, with little dead time. For special calibration runs where one wants to measure the entire waveform, the FEB can also read out up to 32 samples per channel, but at a lower trigger rate. Measuring the energy deposited in each calorimeter channel with excellent resolution over a wide dynamic range of 16 to 17 bits (from tens of MeV to a few TeV per cell) is the primary goal. At the same time, coherent noise is minimized to less than 5% of the incoherent noise, to minimize the effect on physics analysis. The electronics also provide inputs to the L1 trigger at 40 MHz. Performance results from commissioning the L1 trigger system itself are presented elsewhere [10].

The FEB architecture is illustrated schematically in figure 2. The raw signals from the calorimeter are mapped onto the FEB inputs as they emerge from cryostat feedthroughs. On the FEB, the signals are first subject to several stages of analog processing. Preamplifier hybrids terminate the long signal cables from the detector, and amplify the raw signals; three versions of preamplifiers with different impedance and maximum input currents are used to match the detector capacitances and dynamic ranges of the calorimeter sections. In the case of the HEC [11], cryogenic preamplifiers mounted on the detector inside the cryostat provide some amplification of the signals before they reach the FEBs, and the preamplifiers on the FEB are replaced by preshapers that provide a pole-zero cancellation to adapt to the widely varying HEC detector capacitance in order to equalize the pulse shapes before the analog summing that is done for the L1 trigger system. The preshapers invert, amplify and shape the signal so that the signals from the HEC will have the same polarity and approximately the same shape as the signals from the other LAr calorimeters.

The preamplifier or preshaper outputs are split and further amplified by shaper chips on the FEB to produce three overlapping linear gain scales. The gain ratios are $\sim$10 in order to cover the entire dynamic range, with gain values of 1 for low gain, 9.9 for medium gain, and 93 for high gain. Each signal is subject to a fast bipolar CR-$(\mathrm{RC})^2$ shaping function with $\tau = \mathrm{RC} = 13$ ns. The triangular input current pulse from the detector and the output from the shaper are depicted for the case of a typical EMB cell in figure 3. The ionization current for the EMB is approximately 3 μA/GeV, with the actual value depending on η, as shown in reference [1]. The single differentiation of the shaper serves to remove the long tail from the detector response, while the two integrations limit the bandwidth in order to reduce the noise.

The shaped signals are sampled at the LHC bunch crossing frequency of 40 MHz by switched-capacitor array (SCA) analog pipeline chips. The SCAs store the signals in analog form during the

2010 JINST 5 P09003

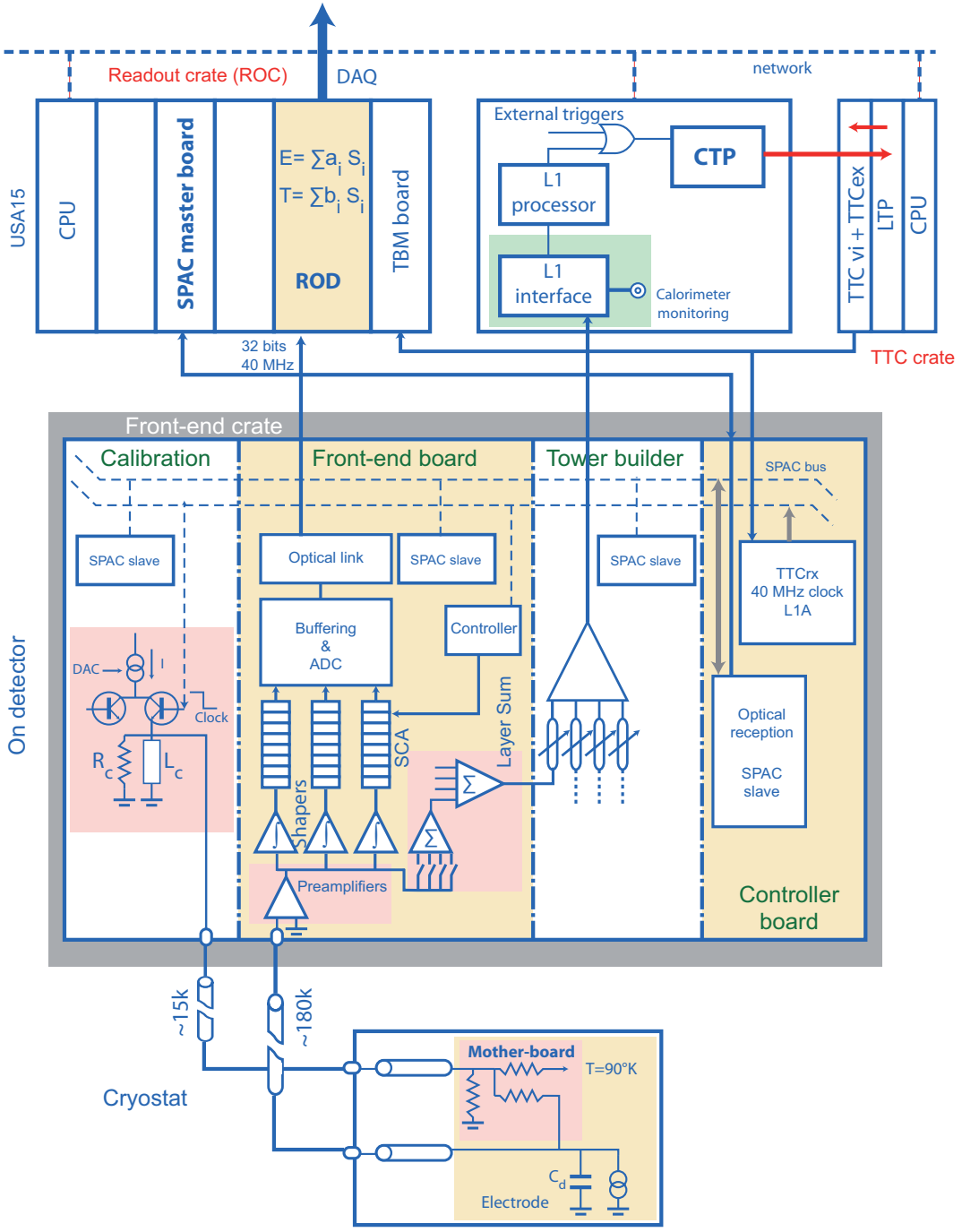

Figure 1. In this schematic drawing depicting the overall architecture of the ATLAS LAr readout electronics, the LAr detectors are located at the bottom. The LAr ionization signal proceed upwards, through the FE crates mounted on the detector to an off-detector processing center called "USA15." Configuration and monitoring in the crate takes place using the Serial Protocol for ATLAS Calorimeters (SPAC). This diagram is valid for the EM calorimeters; slight changes described in the text would be needed to describe the HEC and FCal.

2010 JINST 5 P09003

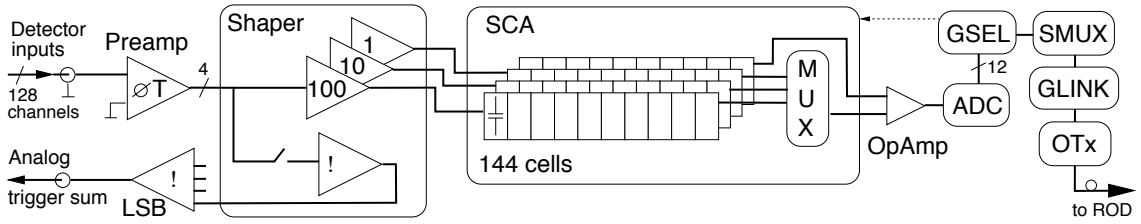

Figure 2. In this schematic block diagram of the FEB architecture, the data flow is shown for four of the 128 channels per board. The data comes from the detectors on the top left. The analog sums exit on the bottom left through the Layer Sum Boards (LSBs) while the digital results are transmitted to the next level of processing through optical transmitters (OTxs) on the right. If these were HEC channels, the preamps would be replaced by preshapers, as described in the text.

L1 trigger latency. For events accepted by the L1 trigger, typically five samples per channel are read out from the SCA and digitized using a 12-bit Analog to Digital Converter (ADC). To optimize the precision of the energy measurement, the Gain Selector chips (GSEL) choose for each channel, in each event, which of the three gains to use, based on the value of the peak sample in the medium gain compared to two reference thresholds. The FEBs can also be configured to read out one or more fixed gains, a feature that is used for certain calibration runs. The digitized data are formatted, multiplexed, serialized, and then transmitted optically from each FEB to the corresponding ROD of the BE electronics.

The RODs, described in more detail in section 7, perform digital processing of the samples for each channel to produce optimized measures of the energy. For channels passing an energy threshold, the time of the deposition and a "quality factor" are also calculated. For those channels passing a second (higher) threshold, the values of the raw samples are also written out, in addition to the results of the processing, to allow additional checks to be performed offline for large energy deposits. The quality factor, defined more precisely in section 7, quantifies whether pulses match expectations or whether they may be mismeasured, for example from waveform distortions produced by energy depositions in neighboring bunch crossings, a phenomenon known as "pile-up".

During development of the electronics, a partial FE system test was performed at Brookhaven National Laboratory (BNL) in 2004 using final prototypes of the various FE boards. Several configurations were tested, the largest of which corresponded to the setup required to read out one "half-crate" of the EMB (including 14 FEBs, one calibration board, and the associated trigger and control boards). This configuration included 1792 readout channels, corresponding to $\sim$1.6% of the channels in the entire EMB, or $\sim$0.9% of the total LAr calorimeter system. The purpose of the BNL test was to verify that the overall FE system met the required performance specifications, before launching production of the various boards. A similar partial system test of the BE electronics was performed at CERN in 2004.

3 Pulse reconstruction and calibration

As depicted in figure 3, a triangular current pulse is produced when charged particles ionize the liquid argon in the high-voltage potential present in the gap between two absorber plates. Once the signal reaches the FEB, a bipolar shaping function is applied and the shaped signal is sampled at

2010 JINST 5 P09003

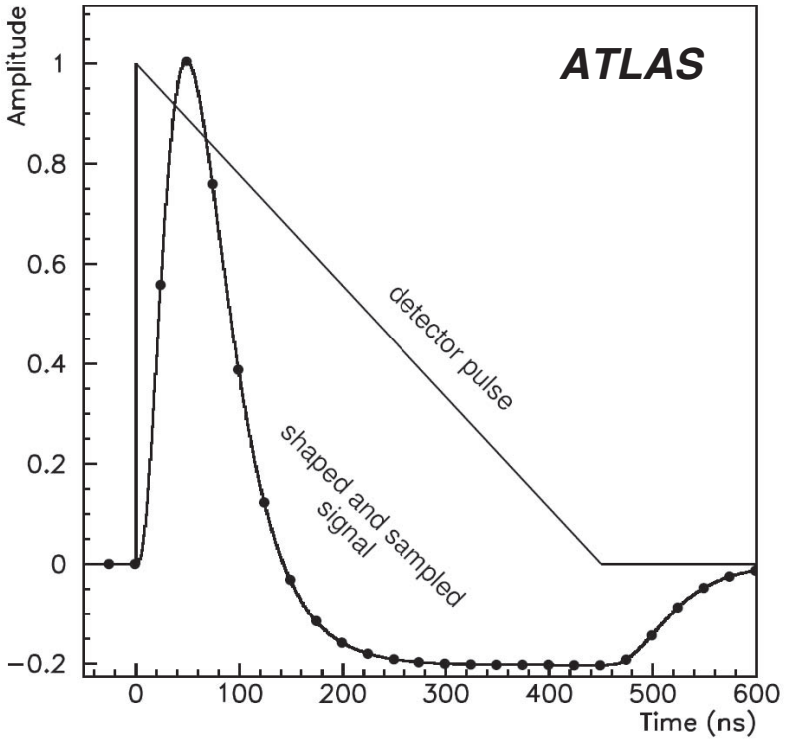

Figure 3. Shapes of the LAr calorimeter current pulse in the detector and of the signal output from the shaper chip. The dots indicate an ideal position of samples separated by 25 ns.

the LHC bunch crossing of 40 MHz. For triggered events, a number of samples $N_{samples}$ per channel is read out. Reading out and utilizing multiple samples provides several advantages, including improving the precision of the energy measurement (as shown below), making the energy measurement insensitive to how accurately a sample can be placed at the top of the peak, and allowing the calculation of other quantities, such as the time and quality factor, in addition to the deposited energy. The typical choice of five samples represents a compromise between the noise reduction achieved and the amount of data that must be digitized and processed in real time.

The ROD reconstructs the amplitude (A) of the signal pulse in ADC counts, as well as the time offset of the deposition (t), by applying a digital filter to the recorded samples (s_j) according to the following equations:

$$A = \sum_{j=1}^{N_{samples}} a_j (s_j - p) \tag{3.1}$$

and

$$t = \frac{1}{A} \sum_{j=1}^{N_{samples}} b_j (s_j - p). \tag{3.2}$$

Here p denotes the pedestal value, namely the mean value of the samples (in ADC counts) when no signal is present. The coefficients a_j and b_j are calculated according to an optimal filtering algorithm [12] that optimizes the resultant energy and timing resolution, and are referred to hereafter as the optimal filter coefficients (OFCs). Calculation of the OFCs uses the expected pulse shape as

2010 JINST 5 P09003

well as the noise auto-correlation matrix for the samples. As this is the total noise, the OFCs will depend on the luminosity, to take into account the noise from the electronics and pile-up together.

It is necessary to convert the reconstructed pulse amplitude A to the deposited energy (E) in MeV. The conversion is performed as follows for the majority of the LAr systems:

$$E = F_{\mu\mathrm{A}\to\mathrm{MeV}} \times F_{\mathrm{DAC}\to\mu\mathrm{A}} \times \frac{1}{\frac{M_{\mathrm{phys}}}{M_{\mathrm{cali}}}} \times \sum_{j=(0,1)}^{N_{\mathrm{ramps}}} G_j A^j \tag{3.3}$$

The factor $F_{\mu\mathrm{A}\to\mathrm{MeV}}$ relates the ionization current in the calorimeter to the energy deposited, and depends on factors such as the sampling fraction of the calorimeter in question. The values for each channel have been determined from test beam data using production calorimeter modules, and validated with a detailed detector simulation. Studies with particles from LHC collisions, and in particular, high-statistics samples of $Z \to e^+e^-$ decays, will be used to determine values which optimize the *in situ* performance for the ATLAS EM calorimeters. The factor $F_{\mathrm{DAC}\to\mu\mathrm{A}}$ converts the Digital-to-Analog Converter (DAC) setting of the calibration board to the injected current, and is determined from known parameters of the calibration boards and injection resistors. The factor $\frac{M_{\mathrm{phys}}}{M_{\mathrm{cali}}}$ quantifies the ratio of response to a calibration pulse and an ionization pulse corresponding to the same input current. The factor G_j is the electronic gain of the channel, which is determined from electronic calibration runs as described later in this section. The sum over j starts from $j = 0$ in medium and low gain only, while in high gain, $j = 1$ is the first term used. The ramp fit polynomial order N_{ramps} is usually 1 such that a linear fit performed, but it can be increased if relevant non-linearity is found in any channel/gain.

As explained below, a series of three types of electronic calibration runs, dubbed Pedestal, Ramp, and Delay runs, provides many of the inputs needed for the cell energy, time and quality factor computations. These runs are taken regularly, usually separately for high, medium, and low gains in order to calibrate all channels and all gains. Typically, a set of Pedestal and Ramp runs is taken daily. A more complete set, including Delay runs, is taken every week. Data are processed automatically and checked daily.

During a Pedestal run, the FEBs are triggered and read out without any input signal present. The pedestal value p for each cell is computed as the average sample value over ∼3000 events recorded with typically 32 samples. The noise is computed as the root-mean-square (RMS) of the pedestal value, while the auto-correlation matrix of the noise, V_{ij}, is computed as

$$V_{ij} = \left\langle s_i \times s_j \right\rangle,$$

where $\langle\rangle$ stands for the mean value over the total number of events.

Figure 4 shows typical noise levels for the first and second layers of the EMB calorimeter, as a function of $N_{samples}$, the number of samples used in the calculation. This result is shown in units of MeV, after the conversion from ADC to MeV, as shown in equation (3.3). Using multiple samples around the peak reduces the noise level, and therefore improves the precision of the energy reconstruction. For the case of five samples, the noise is reduced by a factor of about 1.5-01.8, depending on η, compared to the noise measured using a single sample. This noise reduction is calculated for the case of no pile-up.

2010 JINST 5 P09003

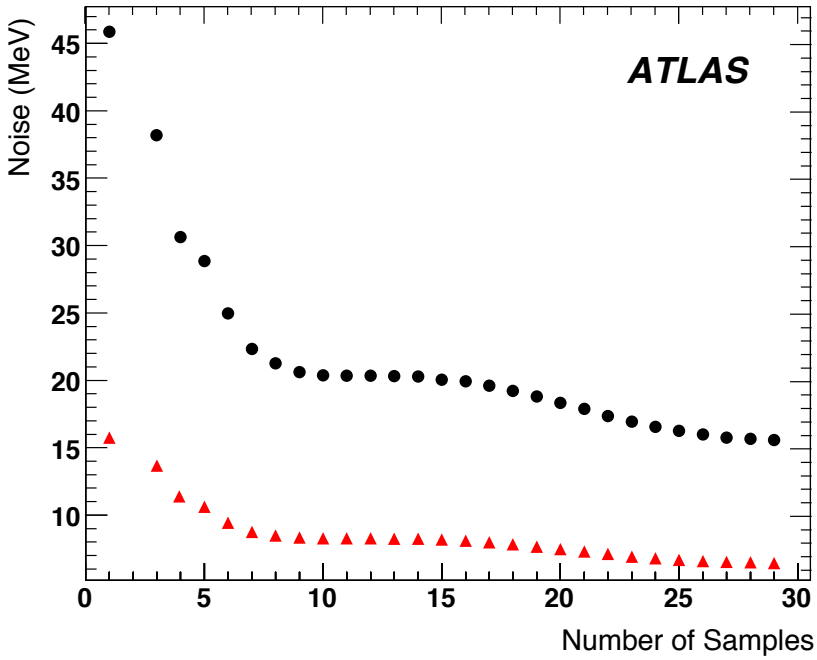

Figure 4. Typical noise levels for the EMB first (triangles) and second (circles) layers as a function of the number of samples used to calculate the deposited energy.

Additional calibration runs use the calibration board to inject precise pulses with programmable amplitudes and delays. The pulse amplitudes are set by programming a precision DAC on the calibration board, and the timing of the pulse can also be programmed. The calibration pulses are injected through precision resistors mounted directly on the detectors inside the cryostat for the EMB and EMEC calorimeters. These calibration signals are exponential before shaping, approximating the triangular ionization pulse.

During a Ramp run, the timing of the pulses is held fixed and a set of typically 100 events is taken with pulses of a fixed amplitude, or DAC value. Different sets of events with different DAC values are taken to map the response over the entire dynamic range. The gain (G) of the readout is determined as the slope of the linear fit of the reconstructed pulse amplitude versus DAC setting. Averaging over the 100 events for each DAC setting improves the precision in the gain determination by suppressing the noise.

For a detailed study of the signal shape, the nominal sampling rate of 25 ns is too coarse. Therefore, during a Delay run pulses of fixed amplitude are injected with various delays with respect to the FEB sampling clock. Typically, 100 events are taken for each delay setting for delay steps of $25/24$ ns each, thereby achieving an effective sampling rate of 1 ns. The shape of pulse produced in response to the calibration pulse is then reconstructed by averaging the events per delay setting and plotting them as a function of the delay. The pedestal-subtracted pulse shapes for one typical EMB channel, as measured from a set of Delay runs with different DAC settings, are shown in ADC counts in figure 5.

Using these calibration data, it is possible to compute OFC values suitable for reconstructing calibration pulses according to the method outlined above, and described in more detail in refer-

2010 JINST 5 P09003

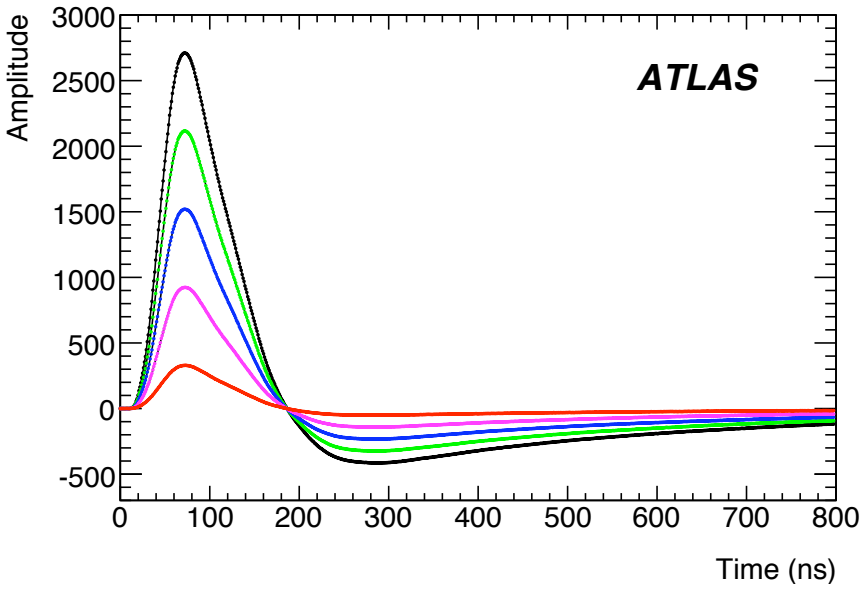

Figure 5. Pulse shapes (measured in ADC counts after subtraction of the pedestal) for a typical channel in the EMB calorimeter as reconstructed using a set of Delay runs, each with a different DAC setting. For more details, see the text.

ences [12, 13]. OFC values suitable for reconstructing ionization signals from particles depositing energy in the calorimeters are calculated in a similar way. However, to obtain a precise description of the ionization pulse shape one must account for the differences in injection point and in shape between the exponential calibration pulses and the triangular ionization pulses, as well as other effects including crosstalk in the calorimeters and electronics, and reflections at the various connectors and interfaces between the detectors and the readout. A precision at the level of $\sim$1% on the ionization pulse is obtained using methods described in detail in references [14, 15], with a corresponding precision on the signal amplitude of $\sim$0.2%. During LHC operations, high statistics samples will allow further cross checks of the understanding of the detailed pulse shapes.

The required calibration constants for each channel, including pedestals and OFC values, are uploaded to the RODs at the start of data-taking, where they are used to process the data read out from the FEBs in real time in order to calculate the deposited energy in MeV, peaking time in units of 10 ps, and the quality factor.

4 Pedestal and noise performance

The pedestal values of all channels are measured frequently as part of the regular calibrations described in the previous section. During LHC running, the pedestal values and noise can be monitored by random triggers in, for example, empty bunch crossings where no collisions are expected. The pedestals are an important input to the pulse amplitude reconstruction; frequent Pedestal runs allow for long term monitoring of the noise and pedestal stability.

In order to allow the negative lobe of the pulse to be measured, the FEB is designed such that each channel has a pedestal value of $\sim$1000 ADC counts. This is important in order to be able to

2010 JINST 5 P09003

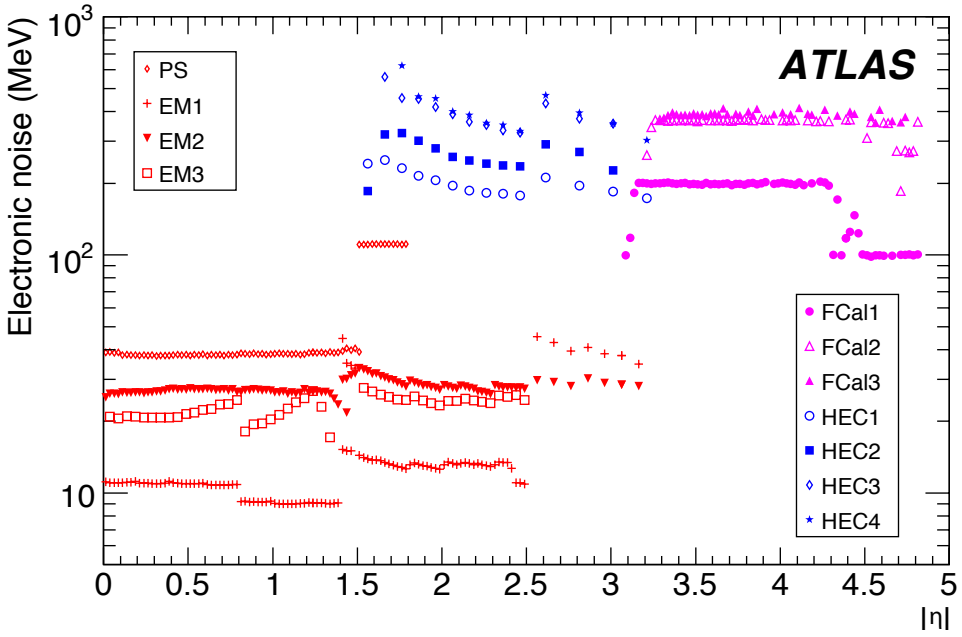

Figure 6. Measured noise (in MeV) for all sections of the ATLAS LAr calorimeters. The PS, and three layers of EM calorimetry make up the EMB and EMEC. The HEC and FCal layers are also shown. The noise values have been averaged over ϕ and $\pm\eta$, as the LAr calorimeter system is symmetric in azimuthal angle (ϕ) and the two halves of the detector (i.e. $+\eta$ and -η) are also symmetric.

measure pulses which, due to pile-up, are sitting on top of the pulses from earlier bunch crossings. Measuring the negative lobe is also critical for measuring the entire pulse in order to determine the drift time [16] which is sensitive to effects that could degrade the calorimeter performance, such as detector construction nonuniformities and the presence of electronegative impurities in the LAr.

4.1 Electronic noise

As part of the quality assurance process during the FEB production, the noise was measured for every FEB before the preamplifiers were installed. The resulting noise values, which include the contributions from the shaper through to the ADC, were typically 0.8 ADC counts (low gain), 0.9 ADC counts (medium gain), and 1.1 ADC counts (high gain).

Once the preamplifiers were installed, typical noise levels were 3–6 ADC counts, depending on the preamplifier type, so the total FEB noise is dominated by the preamplifier contribution. The typical noise per channel increases to 4–10 ADC counts, again depending on preamplifier type, once the detector load is connected.

The noise (in MeV), reconstructed using five samples, is shown in figure 6 as a function of η, separately for each subsystem and layer. These data were taken with the entire calorimeter and electronics system installed in the ATLAS cavern. As can be seen, typical noise levels per channel are $\sim$ 10–30 MeV for the EM calorimeters, which corresponds to $\sim$ 100 nA of equivalent noise current (ENI). For the HEC and FCal, which are more coarsely segmented and have smaller sampling fractions, typical noise levels correspond to $\sim$100–500 MeV per channel.

2010 JINST 5 P09003

4.2 System isolation and noise performance

To ensure good performance of the completed ATLAS detector, ATLAS adopted and enforced stringent specifications for electromagnetic compatibility (EMC) and electromagnetic interference (EMI) among its various subdetectors. The specifications included careful grounding schemes to ensure the isolation of individual systems.

Both the FEB [6] and the FE crate system [4] were designed with careful attention to EMC and EMI issues. During the BNL test, dedicated investigations were performed to evaluate the EMC and EMI behavior of the LAr readout electronics. As described in more detail in reference [17], given that the most troublesome potential source of interference is likely to be near field RF magnetic fields produced by currents in nearby cables, these tests included measuring the coherent noise in the presence of magnetic fields generated by a small loop (about 15 cm in diameter) driven by a 50 W broadband power amplifier and mounted near the FE crate, monitored using a calibrated loop antenna. The power amplifier was driven with the RF output of a network analyzer to sweep over the range from 1 MHz to 40 MHz, with a narrow (100 Hz) filter bandwidth, to evaluate the impact as a function of frequency. The largest impact on the coherent noise was observed for a frequency of 28.5 MHz, due to EMI coupling into the inputs of the preamplifiers mounted on the FEBs. The maximum sensitivity could be characterized approximately as an expected coherent noise of 10% of the total noise per channel for an external field of 1 mA/m at a frequency of 28.5 MHz. Such a field could be generated, for example, from a differential current of 30 mA flowing in a pair of parallel wires mounted a distance of 10 cm from the FE crate. However, in most systems (including those implemented in ATLAS), the wires would be twisted and also shielded, so a significantly higher differential current would be required to generate such a radiated field.

An ATLAS-specific test was performed at BNL by mounting a board emulating the digital output data driver for the Transition Radiation Tracker (TRT) detector near the LAr FE crate. Four TRT cables, each with 20 twisted pairs, were looped on the side of the LAr FE crate, mimicking the location of the TRT cables in ATLAS, where they pass close to the EMB FE crates as they exit the detector. The effect on the FEB performance of the EMI emitted from the TRT cables was extremely small, with an increase of the coherent noise of $\sim 0.3\%$ per channel for 20 MHz data transmission, and only $\sim 0.08\%$ per channel at 40 MHz. The effect of the operation of the FEBs and other LAr FE electronics on the TRT bit error rate was also studied, but was so small as to not to generate any errors during a run of 60 hours at 40 Mb/s, corresponding to a limit of the bit error rate of less than 10^{-14}.

Dedicated tests were performed in the ATLAS cavern to investigate the EMC and stability of the DC power distribution system used for the LAr readout, which includes AC/DC converters that are located outside the detector hall in USA15. Long cables from USA15 are used to drive DC/DC converters located close to each FE crate on the detector. The tests, described in detail in reference [18], included studies that demonstrated the guaranteed stability of the power distribution system, and measurements of common-mode and differential-mode noise along the power cable, as well as of EMI emissions of the power cable.

The grounding and isolation scheme implemented for the LAr calorimeters as installed in the ATLAS cavern is discussed in detail in reference [4]. As explained there, the shields of the high voltage (HV) cables are connected on the side of the USA15 ground but were originally

2010 JINST 5 P09003

disconnected at the cryostat end. However, during commissioning tests in the ATLAS cavern, large high frequency noise signals were observed in the LAr readout, especially for the PS channels. The source of the noise was established as an AC potential difference between the USA15 ground and the cryostat ground, which was entering the cryostats by coupling to the HV cables. The installation of a 1 μF capacitor between the shield of the HV cables (USA15 ground) and the HV filter ground (cryostat ground) cured this noise problem.

4.3 Coherent noise

Given the fine granularity of the LAr calorimeter, typically 50–100 calorimeter cells are summed to measure the energy of an electron or photon, and even more channels must be summed for a typical jet or for more global quantities such as missing transverse energy (MET). Therefore, minimizing the coherent noise is particularly critical, and the specifications of the LAr readout require that the coherent noise be kept below 5% of the incoherent noise.

In the BNL test, the coherent noise within one FEB was measured by comparing the RMS noise of the digital sum of n channels with the square root of n times the average RMS noise per channel. The quadratic difference is a measure of the coherent noise. The measurements showed that the coherent noise per channel was less than 2% of the incoherent noise. For larger sums, such as over the 14 FEBs in the BNL crate test, the coherent noise dropped even further, to less than 1% of the incoherent noise.

The coherent noise is particularly sensitive to the grounding and isolation conditions. For example, at one stage during detector commissioning in the ATLAS cavern, a large coherent noise contribution was observed for one octant of the PS in the EMB. Investigations revealed that a HV cable feeding this octant had a broken shield, caused by a broken connection to the 1 μF capacitor. The noise problem was cured once the faulty HV cable was replaced with a spare.

The coherent noise analysis was repeated to determine the *in situ* performance as measured for the calorimeters installed in the ATLAS cavern. Figure 7 shows that the level of coherent noise per channel within the second layer of the EMB is typically 2–3%. The second layer is especially important, as it contains the largest part of EM showers. The coherent noise is also low in the first and third layers, about 6% and 2% respectively. These levels are per FEB, while data from more than one FEB will be used when constructing clusters of energy, further reducing the coherent noise. The combination of the intrinsic FEB performance plus the effectiveness of the EMC/EMI measures described in the previous section has led to excellent *in situ* coherent noise performance.

4.4 Pedestal and noise stability

The stability of the pedestal, noise and auto-correlation values has been monitored over extended periods of time, using data taken with the complete detector. Sample results as measured over a period of about six months in early 2009 are shown for the EMB and EMEC together in figure 8. The HEC and FCal have similar stability results.

The stability is further quantified in table 1. For example, typical variations in pedestal values for single channels are at the level of 0.02 ADC counts. This corresponds to an energy of about 1 MeV for the medium gain of the EMB and EMEC, about 2 MeV for the HEC and 10 MeV for the FCAL. Noise variations are typically less than 0.01 ADC counts for high gain in the EM calorimeters, $\sim$ 0.02 ADC counts in the FCal, and an order of magnitude less for medium and low gains.

2010 JINST 5 P09003

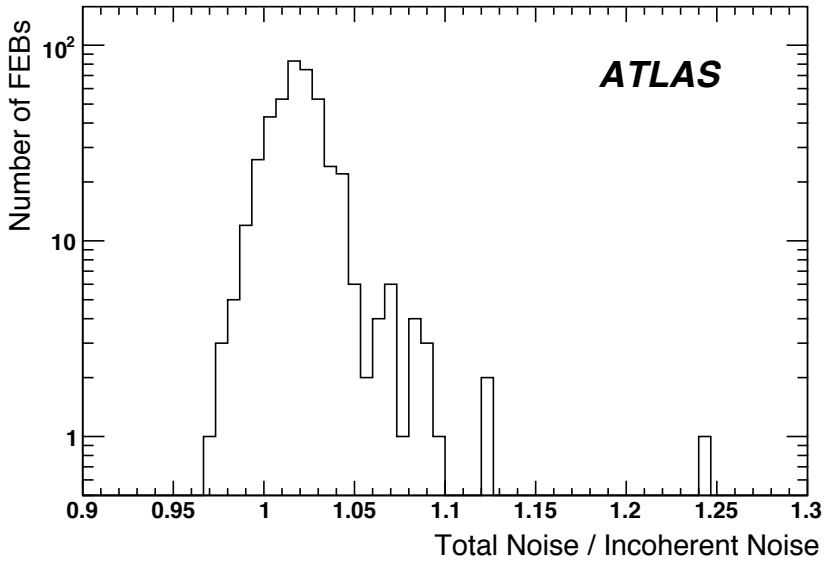

Figure 7. The ratio of total noise to incoherent noise for the middle layer of the EMB is shown, with one entry per FEB for 432 FEBs. If there were no coherent noise, the ratio would be equal to unity. The mean of the distribution is 1.021.

Table 1. Table displaying the stability of various calibration quantities measured over a period of approximately six months, for all three gains and for each of the calorimeter subdetectors. (Data is not taken in high gain for the HEC.) ΔPed is the difference (in ADC counts) between the mean pedestal for all 128 channels of a given FEB as calculated in a given pedestal run versus as calculated in a reference run. ΔNoise is a similarly calculated quantity, but for the difference in the mean noise per channel (in ADC counts). The change in the mean gain, given by Δg/g, is calculated in a similar way, as described in the text. For each quantity, the RMS is shown for the histogram of all FEBs and all runs over this six month period, as well as the value of σ determined from a Gaussian fit.

		EMB+EMEC		HEC		FCal	
Gain	Quantity	RMS	σ	RMS	σ	RMS	σ
High	ΔPed[ADC]	0.025	0.023			0.022	0.019
	ΔNoise[ADC]	0.007	0.003			0.029	0.023
	Δg/g[%]	0.050	0.024			0.009	0.009
Medium	ΔPed[ADC]	0.022	0.021	0.021	0.018	0.019	0.017
	ΔNoise[ADC]	0.001	0.001	0.010	0.002	0.075	0.002
	Δg/g[%]	0.048	0.013	0.084	0.071	0.007	0.007
Low	ΔPed[ADC]	0.022	0.021	0.019	0.016	0.017	0.014
	ΔNoise[ADC]	0.001	0.001	0.001	0.001	0.001	0.001
	Δg/g[%]	0.050	0.018	0.074	0.053	0.006	0.005

2010 JINST 5 P09003

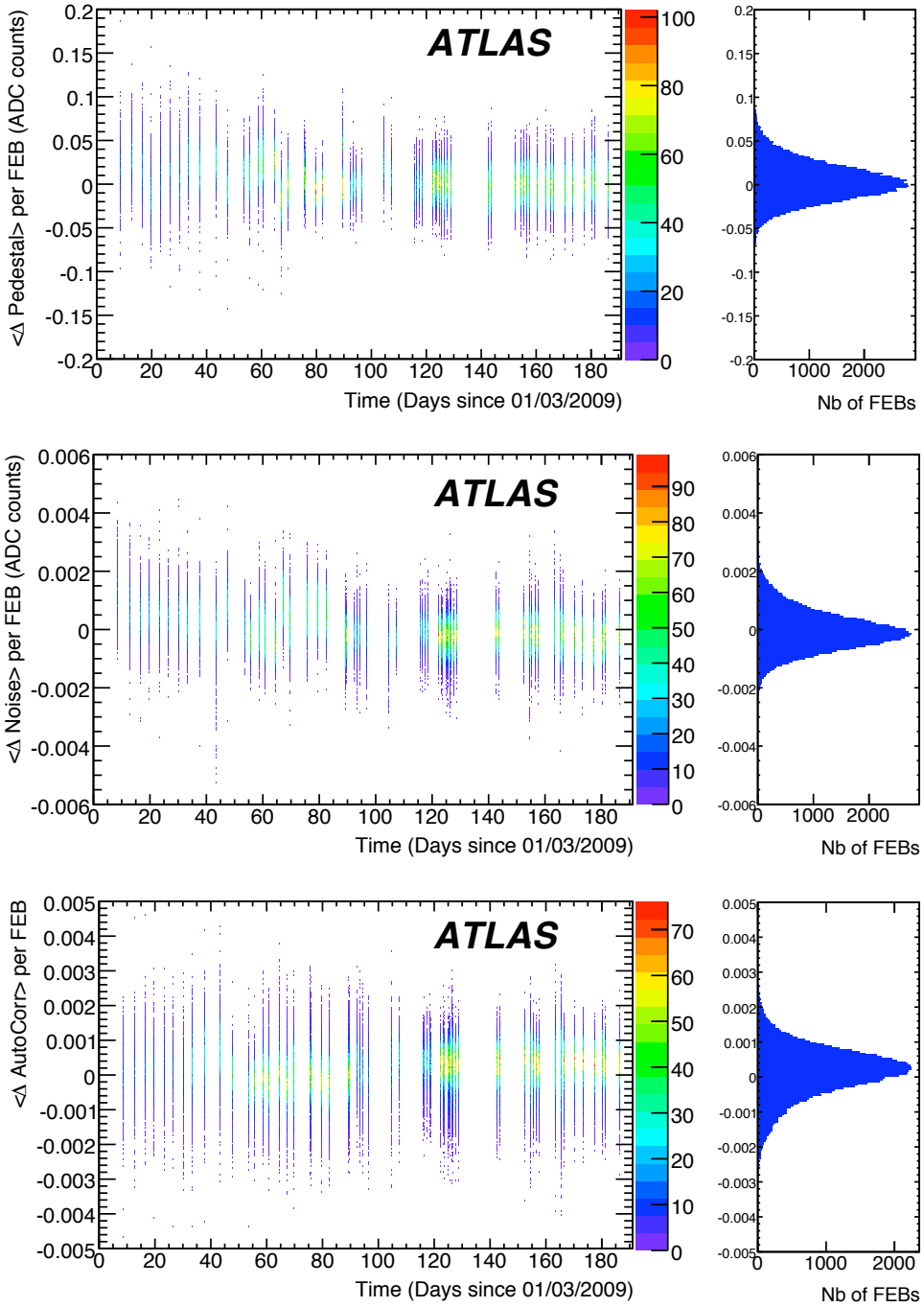

Figure 8. Stability of EM pedestal, noise and auto-correlation values from about 60 Pedestal calibration runs over a period of six months, here shown for medium gain. The pedestal (upper figure), noise (middle figure) and auto-correlation values (lower figure) are compared for each channel with the corresponding values from a reference run. The average change for each FEB is plotted versus elapsed time.

5 Energy measurement

Providing precise energy measurements over the range of MeV to TeV is the central task of the LAr calorimeters and readout. For low energies, the measurement error should be dominated by

2010 JINST 5 P09003

the noise. The calibration of the calorimeter readout should be understood at a level of precision of 0.25% to control the overall constant term in the energy resolution function, as defined later in equation (5.1).

Since analog summing is used to make the L1 trigger towers, meeting the specified trigger performance requires that channels within a given analog sum have an energy response which is uniform within 5%. The preamplifier gains are, in fact, uniform to within 1–2% [6], exceeding this specification.

5.1 Energy resolution of the electromagnetic calorimeter

Ramp runs can be used to determine the contribution of the electronics to the resolution for reconstructing the energy deposited in a channel. Figure 9 shows the relative energy resolution, $\sigma(E)/E$, versus energy for a representative channel in the second layer of the EMB calorimeter. The plot superimposes results for all three gain scales. The value used for σ of a given point is the RMS, calculated over 100 pulses, of a single sample measured at the peak of the pulse.

The data are compared to an estimate of the energy resolution in one cell with the form of the curve given by:

$$\frac{\sigma(E)}{E} = \frac{a}{\sqrt{E}} \oplus b \oplus \frac{c}{E} \tag{5.1}$$

where the energy is measured in GeV and $\oplus$ indicates addition in quadrature. For the purpose of this comparison, $a = 10\%$, which is the typical stochastic term for an electromagnetic shower, $b = 0.25\%$ for the local constant term, and $c = 45$ MeV is the noise measured from a single sample for the considered cell in high gain. The second, "constant," term dominates at high energy, so it especially important to minimize. Here, $b = 0.25\%$ is the specification for the local constant term, applicable to a single channel with the aim of limiting the global constant term across the entire calorimeter to less than 0.7%. In test beam studies before the final system was installed, a sampling term of 10% and local constant term of 0.17% were measured for the EMB [19].

The high gain signal, which is used to reconstruct relatively low energies, is applicable up to about 25 GeV, after which it saturates. The values of σ for the high gain are dominated by the noise, which is about 45 MeV for a single sample for this particular channel. Therefore, the resolution improves roughly like $1/E$, reaching a level of 0.2% for energies near 25 GeV.

The resolution for medium gain is just under 0.4% at the energy of 25 GeV, where it takes over from high gain. The medium gain resolution improves roughly like $1/E$ until saturation is reached near 250 GeV, where the resolution is below 0.07%.

For higher energies, the low gain readout would be used. The low gain has a resolution below 0.4% at the crossover point of 250 GeV, and then improves roughly like $1/E$ to provide a resolution better than 0.07% for the highest energies, in the 1–2 TeV range.

Since the RMS of a single sample is used for the σ values in the figure, the results shown do not take into account the improvement by a factor 1.5–1.8 that is achieved in suppressing the noise by using OFCs from five samples, as described previously (see figure 4). As the points shown for this channel are in units of energy, rather than ADC counts, factors to convert from DAC to μA and μA to MeV have been applied. Figure 9 demonstrates that the energy resolution of the LAr electronic readout does not significantly contribute to the overall energy resolution.

2010 JINST 5 P09003

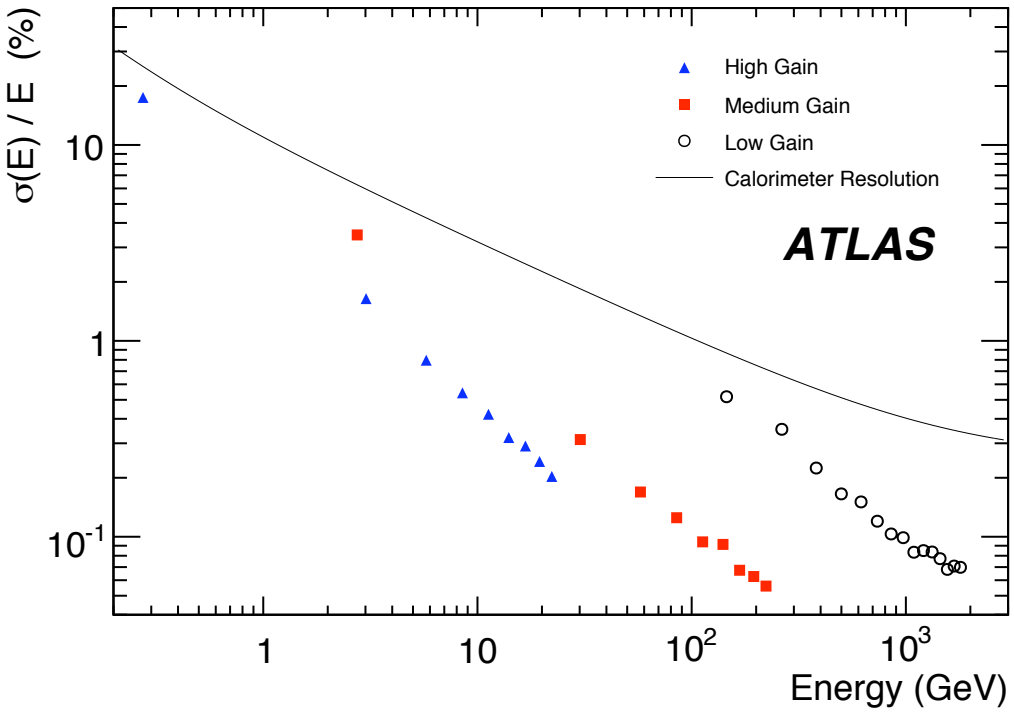

Figure 9. Energy resolution versus energy of a representative EMB second layer channel, as measured during Ramp runs. The points represent the data, while the solid curve shows a parametrization of the total calorimeter energy resolution, given by equation (5.1). For more details, see the text.

5.2 Linearity

Ramp calibration runs are used to determine the linearity for reconstructing the energy deposited in a channel. Figure 10 shows the integral non-linearity (INL) versus energy for the same channel of the second layer of the EMB as in figure 9. The plot superimposes results for all three gain scales. The INL is defined at each point i and for each gain as

$$\mathrm{INL}_i = (E_{measured,i} - E_{fit,i})/E_{max}. \tag{5.2}$$

Here, $E_{fit,i}$ is the result for point i of a straight-line fit to all the data points of the gain in question, while E_{max} is the value of the maximum energy point used for that gain.

The results indicate that the readout electronics are linear to typically 0.2% or better, including the combined effects of both the FEB that measures and reads out the calorimeter signals and the calibration board that generates and injects calibration pulses.

5.3 Stability of the energy measurement

The stability of the gain of the LAr readout can be studied by comparing the results of calibration runs taken over an extended period of time. Figure 11 shows the fractional change in gain for the medium gain readout of the EMB and EMEC. It has been obtained from an analysis of Ramp runs taken over a period of six months in early 2009. The stability of the measured gains for the various calorimeters was summarized in table 1. The variations with time are typically within

2010 JINST 5 P09003

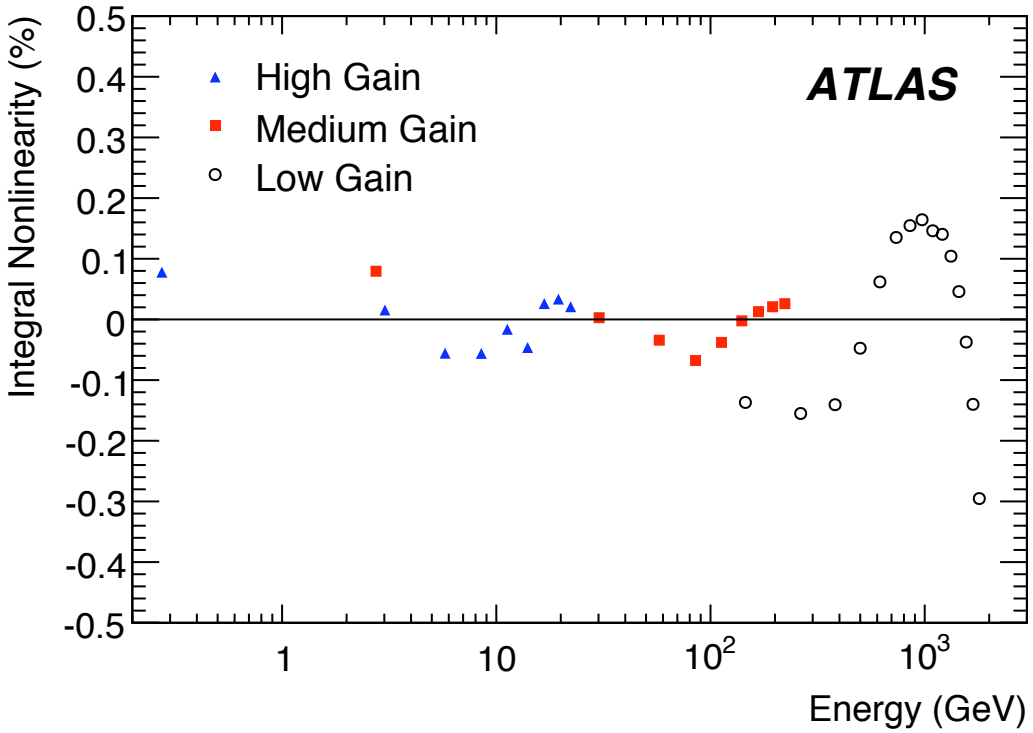

Figure 10. Integral non-linearity (INL) versus energy of a representative EMB second layer channel, as measured during Ramp calibration runs.

0.3%, demonstrating that the readout gains are very stable. During operation of ATLAS, frequent calibration runs will be performed and even such small variations will be taken into account.

5.4 Crosstalk

During the BNL test, the FEBs were not connected to the LAr detectors but to a set of boards mounted with capacitors that were produced for the test in order to mimic the detector loads. As part of these tests, the crosstalk intrinsic to the FEBs was measured by pulsing individual channels and examining the signals in neighboring channels. The results demonstrate that the crosstalk between neighboring FEB channels is typically less than 0.5%, dominated by capacitive coupling in the FEB input connectors. This effect is small compared to the crosstalk in the LAr calorimeter signals induced by capacitive couplings within the structures of the calorimeters themselves. Depending on the calorimeter section, the crosstalk can amount to several percent, with the highest crosstalk of 4–7% in the EM calorimeter within the first layer. The second and third layers have a crosstalk of $\sim$1%. These are within the specifications and will not adversely affect the energy resolution. More information about how the reconstruction takes crosstalk in the detector into account can be found in the references [15].

6 Time measurement

As described in section 2, along with the energy calculation, the time of the energy deposition is also computed for every channel with energy above a specified threshold. The LAr timing

2010 JINST 5 P09003

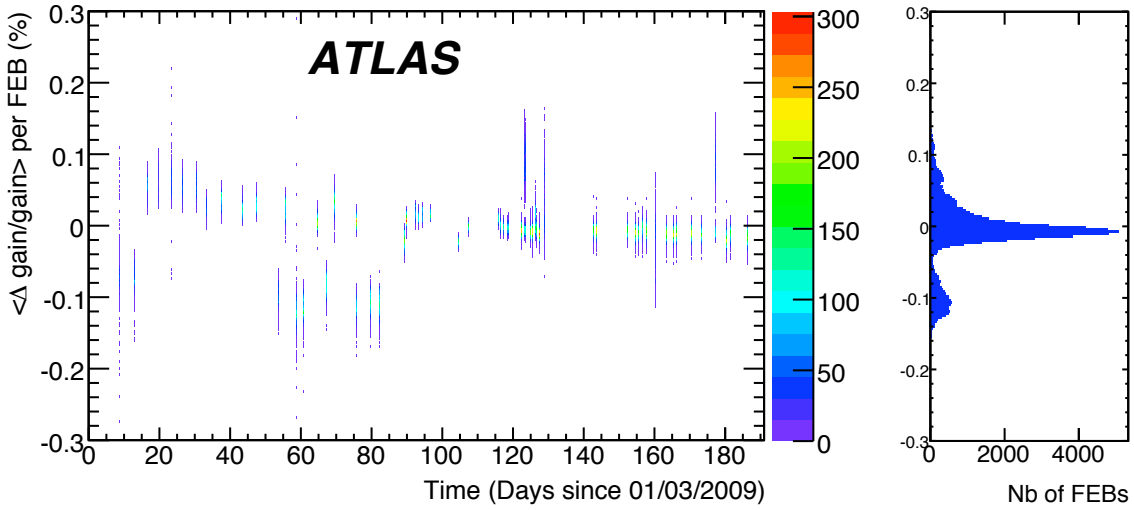

Figure 11. Stability of EMB and EMEC gain values from about 60 calibration runs over a period of six months, shown for the medium gain. The gain is compared for each channel with a reference run. The average change, normalized to the gain value of the reference run, is plotted for each FEB. The outliers seen in the plot are still under study; they are not correlated to temperature or the magnetic field.

measurement is important for several reasons. Good understanding of the timing helps distinguish between energy deposits resulting from the triggered beam crossing and those from neighboring bunch crossings. The longitudinal segmentation and timing can also be used together to identify non-pointing photons [20].

During 2001–2002, test beam measurements on production EM calorimeter modules were performed as part of their qualification process. An analysis of the LAr calorimeter timing resolution was performed using this data. These studies demonstrated that a constant term in the timing resolution of order 100 ps is achievable for electrons. The analysis also demonstrated that the contribution to the constant term from the readout electronics itself was only ∼20 ps [21]. However, these measurements were made using early prototypes of the FEB and calibration boards which did not include the final clocking scheme that is implemented in ATLAS. It is necessary, therefore, to repeat such an analysis using the final, production versions of the electronics.

6.1 Time resolution

During Delay runs, the full waveform is reconstructed in response to calibration pulses, as described in section 3. The pulse shape data includes measurements of the average amplitude of the pulse at each time point, as well as the RMS over the typically 100 events averaged for that particular delay setting. Reconstruction of the pulse shape in bins of 1 ns, as shown in figure 5, also allows numerical computation of the time-derivative of the pulse.

The measured RMS at a particular time value has a contribution due to the noise, which should be independent of time, and a contribution due to the timing jitter, which is dependent on the derivative of the pulse shape evaluated at that time. Taking a Gaussian approximation, this may be

2010 JINST 5 P09003

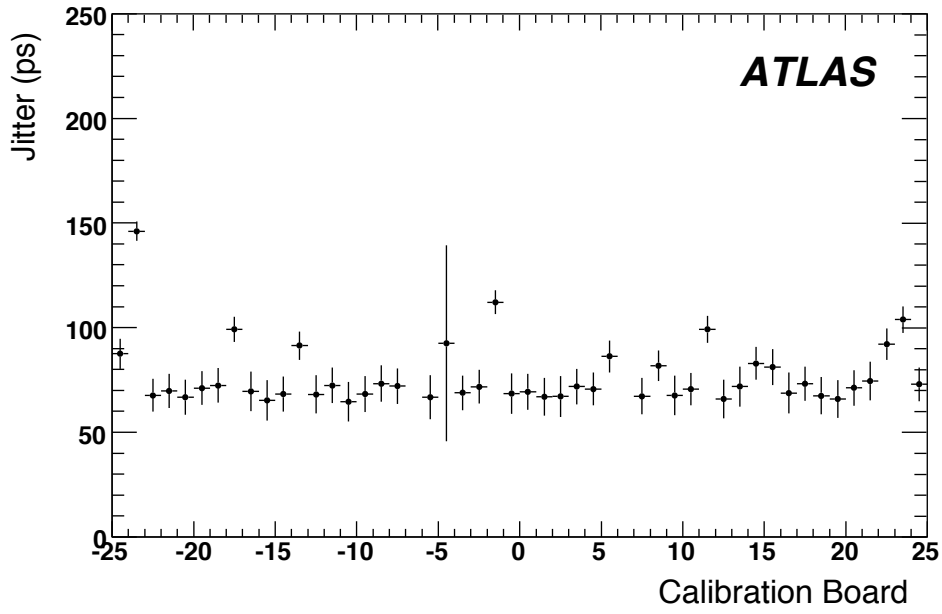

Figure 12. Jitter for the EMEC for calibration runs. As explained in more detail in the text, the jitter for data taken from LHC collisions will be less than for calibration runs.

expressed quantitatively as:

$$\sigma^2_{total} = \sigma^2_n + \left(\frac{df}{dt}\right)^2 \times \sigma^2_t$$

where σ_n is the single-sample noise level, σ_t is the timing jitter, and $\frac{df}{dt}$ is the time-derivative of the pulse shape $f(t)$ evaluated at that time. Therefore, studying the total signal spread, σ_{total} as a function of the time-derivative, which varies at different points on the pulse, allows a determination of the timing jitter.

Figure 12 shows the jitter determined from calibration signals for all the calibration boards in the EMEC. The typical jitter is around 70 ps.

On the calibration board, the 40 MHz clock is received and recovered by the custom TTCrx ASIC [22], and this clock is used to trigger the calibration pulse. Previous studies have demonstrated that the jitter from the TTCrx chip itself is sufficient to explain the values seen in figure 12.

As described previously, the calibration system is used to make the measurements required as input for the determination of the OFC values used for reconstructing ionization pulses. Jitter in the calibration pulses has negligible impact on the pulse reconstruction in Ramp and Delay runs, because 100 events are typically averaged. While there are variations seen from one calibration board to another, the typical jitter values are low enough that they will not significantly impact the determination of the OFC values.

The readout via the FEB alone has lower jitter. While it also uses the TTCrx for clock recovery, the FEB design incorporates a dedicated component, the QPLL [23], to reduce the jitter on the TTCrx clock. This was necessary to guarantee stable operation of the 1.6 Gbps optical link used on each FEB to transfer the data to the RODs, whose driving clock must be generated by multiplying

2010 JINST 5 P09003

up from the 40 MHz input clock. An additional benefit of the QPLL is that the jitter reduction also translates to better timing resolution for the readout of LAr ionization signals (where the calibration board is not involved). During production qualification, the jitter of each FEB was measured [6] and was required to be less than 20 ps. Typical values are 10 ps or less.

6.2 Time uniformity

The FEB is designed such that one overall time offset per FEB can be programmed. This allows the sampling phase to be adjusted in order to, for example, place a sample near the expected peak of the shaped calorimeter signals.

The relative timing of the ionization signals in various calorimeter channels can be predicted from the timing information measured in calibration runs by applying corrections for effects such as the time-of-flight of the particles from the collision point and various cable lengths. As detailed in reference [3], such an analysis has been performed and compared with the timing results as obtained from cosmic ray data and first beam events. The agreement between the prediction and the measurements is within ± 2 ns in the EM and HEC calorimeters, and within ± 5 ns for the FCal. With first collisions, the timing of illuminated cells has been verified at the level of ± 1 ns.

7 Performance of the Back End electronics

The LAr Back End (BE) system [5] is responsible for communicating with the FE crates, receiving, monitoring and digitally processing the calorimeter data from the FEBs, as well as communicating with the ATLAS trigger system.

The main component of the BE system is the ROD, which receives signals from the FEBs over approximately 70 m optical fibers. A ROD is connected to up to 8 FEBs, processing a maximum of 1024 channels. A ROD holds four Processing Units (PUs), each with two Digital Signal Processor (DSP) blocks, such that one DSP block is responsible for processing the data from one FEB. The ROD checks, processes, and formats the data coming from the FEBs. As the raw data will generally not be recorded offline, monitoring histograms are also important to help verify the output. RODs send their output signals through optical fibers to the next level of the ATLAS trigger and DAQ system.

The computations performed by the DSP must meet stringent requirements for processing time, memory, and bandwidth. During LHC collision data-taking, the RODs must process the data with a L1 trigger rate up to 75 kHz, implying an average of 13 μs per event for data processing. During calibration runs, the trigger rate is much lower, only a few 100 Hz.

7.1 Digital signal processing

The main function of the LAr ROD DSP block is to process the calorimeter data which has been digitized and read out by the corresponding FEB. The optimal filtering algorithm is applied by the DSP to calculate the deposited energy from the calorimeter samples. For any cell that passes a programmable energy threshold, the time of the deposition and the quality factor are also calculated. For cells passing a second threshold, all the samples of the signal are read out, in addition to the processed quantities.

2010 JINST 5 P09003

Each ROD DSP block includes an Input FPGA (InFPGA), a DSP, and an Output FIFO. The InFPGA receives and parallelizes the incoming FEB data, and verifies its integrity (by performing parity and other data consistency checks) to detect possible data corruption due to single event upsets or other effects. Using 32 kbits of its embedded memory, configured as a dual-port memory, the InFPGA stores the FEB data before its transmission to the DSP. This memory is separated into two banks, to one of which incoming data is written, while the other is read out by the DSP. The memory is configured as Random Access Memory (RAM) to allow the incoming data to be written to non-consecutive addresses. This reorganization of the incoming FEB data allows optimization of its use by the DSP processing algorithm, so that the memory is seen by the DSP as a FIFO. Once a complete FEB event is stored in the memory, or if the number of words written in the bank reaches the data block size set by the DSP, the InFPGA sends an interrupt to the DSP which launches a direct memory access to read the event.

The 720 MHz TMS320C6414GLZ is a high performance fixed-point DSP, executing up to 5.7×10^9 instructions per second. The core processor has 64 general purpose 32-bit registers and eight independent functional units: two multipliers for a 32-bit result and six arithmetic logic units. The DSP peripherals include two glueless external memory interfaces (EMIF), configured as a synchronous memory interface. The first EMIF, the 64-bit wide "EMIFA" is used to input FEB data, whereas the second 16-bit wide "EMIFB" is used to output the results of the DSP processing algorithms. The DSP uses a two-level cache-based architecture. The Level 1 cache consists of a 128 kbit program memory and a 128 kbit data memory. The Level 2 cache consists of an 8 Mbit memory which is shared between program and data. This memory is used to store the DSP software, the input and output data buffers, histograms, and calibration constants. A dedicated memory map, as well as pipelined memory accesses, are used to optimize the performance when accessing data. To decrease the software complexity and simplify its legibility and maintenance, the DSP code is written in C and optimized by the compiler.

In the following discussion, the computation will be described for the typical case of five samples being read out. To process each event in the allowed time, the input data, calculation algorithm, and output of the DSP computations are optimized. To streamline the calculation of the deposited energy, equation (3.3) can be re-written as:

$$E = F_{ADC\rightarrow \text{MeV}} \times A = \sum_{j=1}^{5} \alpha_j s_j - P_a \tag{7.1}$$

where the factor $F_{ADC\rightarrow \text{MeV}}$ combines the various multiplicative factors in equation (3.3), and we introduce the definitions that $\alpha_j = F_{ADC\rightarrow \text{MeV}} \times a_j$ and P_a is defined in table 2. The G_0 term in equation (3.3) for the medium and low gain in the EM and low gain in the HEC is absorbed into the new definition of the pedestals (P_a). In a similar manner, equation (3.2) can be rewritten as:

$$E \times t = \sum_{j=1}^{5} \beta_j s_j - P_b \tag{7.2}$$

with $\beta_j = F_{ADC\rightarrow \text{MeV}} \times b_j$ and $P_b = F_{ADC\rightarrow \text{MeV}} \times p \sum_{j=1}^{5} b_j$. Since the divide operation required to calculate the time from equation (7.2) does not map efficiently onto the fixed-point DSP, the inverse of the energy is instead retrieved from a Look-Up table (LUT) and used to obtain the time:

$$t = (E \times t) \times \text{LUT}(E - G_0') \quad . \tag{7.3}$$

2010 JINST 5 P09003

Table 2. Packed calibration constants and scales that are loaded in the DSP for use in the calculations of the deposited energy, time and quality factor. Most of them are defined in the text. The scales n_a and n_b are not calibration constants, they are scales (2^{n_X}) by which the constants are multiplied have 16-bit integers. They are themselves coded on 16 bits. The "G'_0" constant is the gain factor (G_0) with conversion factors applied. The predicted pulse shape, g_j, with the maximum normalized to 1, is used in the definition of h_J.

Constant	Formula	Number/channel/gain	Format
α_j	$a_j \times F_{ADC\rightarrow \text{MeV}}$	5	16-bit integer
n_a	–	1	16-bit integer
β_j	$b_j \times F_{ADC\rightarrow \text{MeV}}$	5	16-bit integer
n_b	–	1	16-bit integer
P	p	1	16-bit integer
P_a	$\sum_j \alpha_j (p - \frac{G'_0}{\sum_j \alpha_j})$	1	32-bit integer
P_b	$p \sum_j \beta_j$	1	32-bit integer
h_j	$g_j / F_{ADC\rightarrow \text{MeV}}$	5	16-bit integer
Total number per channel		$22 \times 3 = 66$	
Size per channel		1152 bits	

The LUT is implemented as a table of 16-bit words and requires a total memory allocation of 4 kBytes. G'_0 is zero for high gain in the EM, and medium and high gain in the HEC; for the other gains it is G_0, converted into energy units.

The quality factor Q compares the results from the measured samples and the expectation for the pulse as defined here:

$$Q = \sum_{j=1}^{5} \left(s_j - p - (E - G'_0) \times h_j \right)^2 \quad . \tag{7.4}$$

The constants h_j are calculated as samples at the appropriate time positions on the expected pulse shape, normalized to unit pulse height, and G'_0 if defined as explained above.

To optimize the processing time, the calibration constants are stored in the DSP in the same order as the samples coming from the FEB. Optimization for memory usage is also important. The conditions database containing the LAr calibration constants is one of the greatest memory consumers in ATLAS. The calibration constants used to compute the energy, time and quality factor in the DSP are prepared and packed in integer formats. A summary of all of the constants that are loaded into the DSP, and the formats used, is given in table 2.

While the ROD input bandwidth is determined by the FEB output and the preprocessing done before the DSP on the ROD, the output bandwidth is a result of the DSP computations and output data formatting. To comply with both bandwidth and data reduction requirements, the DSP algorithms must minimize the amount of data without losing significant information. The value of the calculated energy is packed into 16 bits (13 bits of mantissa, 2 bits of range and 1 bit of sign). The time is packed as a signed 16-bit integer, and the quality factor is packed as an unsigned 16-bit integer. For the energy and time calculations, the numerical precision is given by the value of the least significant bit (LSB). This corresponds to 10 ps for the time. The LSB for the energy,

2010 JINST 5 P09003

Table 3. Numerical precision for the energy calculation implemented in the DSP.

Energy Range	Numerical precision
$\|E\| \leq 2^{13}$ MeV $= 8192$ MeV	$\Delta E \leq 2^{0}$ MeV $= 1$ MeV
$2^{13} < \|E\| \leq 2^{16}$ MeV $= 65536$ MeV	$\Delta E \leq 2^{3}$ MeV $= 8$ MeV
$2^{16} < \|E\| \leq 2^{19}$ MeV $= 524288$ MeV	$\Delta E \leq 2^{6}$ MeV $= 64$ MeV
2^{19} MeV $< \|E\|$	$\Delta E \leq 2^{9}$ MeV $= 512$ MeV

and therefore the precision, is energy-dependent (as shown in table 3) but always much lower than the calorimeter energy resolution, to avoid making a significant contribution to the overall energy uncertainty. Given the definition of Q, its numerical precision is proportional to $\sqrt{Q}$.

Special runs have been taken, with both the raw data and the results of the DSP calculations read out, to validate the DSP computations by allowing a comparison of the DSP results with those computed offline. For all three quantities, the numerical precision of the DSP computation is as expected.

7.2 Processing time

Figure 13 shows an oscilloscope trace indicating the time required for the various stages of the processing of the FEB data.

First, in step A, the energy deposited in each of the 128 channels is calculated by applying the optimal filtering algorithm to the five samples per channel. This step takes 3.8 μs to complete - the time between the shorter pulses. It is followed in steps B and C by the filling of histograms. Then the total energy and energy projected along the x, y, and z axes are calculated in step D, as inputs to global energy and missing energy sums in the Level 2 trigger. For those cells above an energy threshold (25% of the channels in the example shown), the time and the quality factor are then determined in step E. In addition to the processed data, the raw samples are also output in step F for channels above a higher energy threshold. Finally, in step G the DSP calculates a checksum that is used offline to verify the data integrity. The total processing time for all the operations is 9.6 μs, which is low enough to meet the requirement of 13 μs of processing time for 75 kHz L1 triggers.

It is important that the system performs robustly, by asserting a Busy state, should the L1 trigger rate exceed the expected maximum rate. During dedicated system tests, the LAr electronics functioned well with an input rate of 157 kHz and a L1 output rate of 85 kHz. This test demonstrates that the system will be able to effectively process data at the required rate and above it, when high-rate fluctuations occur.

8 Summary

A system of custom electronics has been developed for the readout of the ATLAS LAr calorimeters. To meet the ATLAS physics goals, the readout faced a set of demanding specifications. Using the results of calibration runs taken after the full detector was installed at CERN, it has been demonstrated that the electronics meets or exceeds the required performance. The readout performs for,

2010 JINST 5 P09003

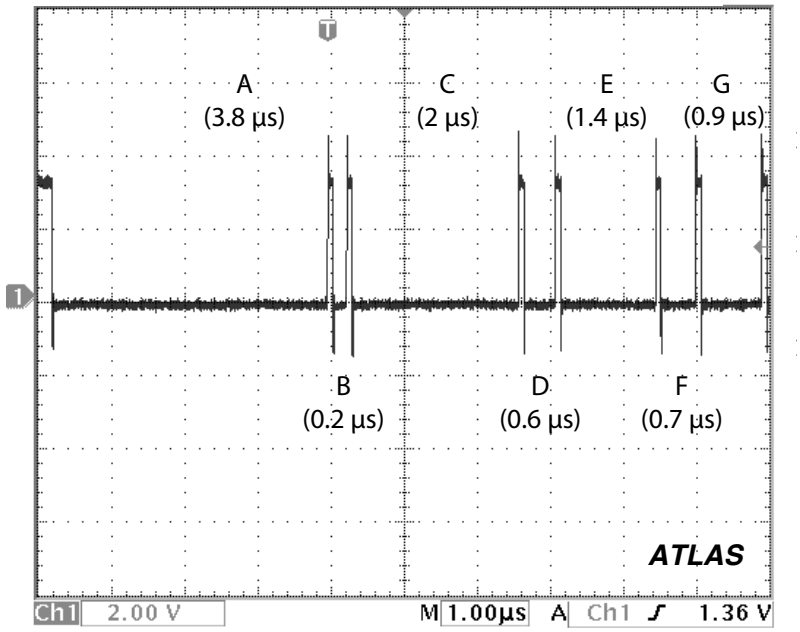

Figure 13. An oscilloscope trace showing the time required for the various stages of the DSP processing of one event of FEB data, with five samples per channel. The time for each stage of the processing (between the pulses) is shown on the figure, while the labels are defined in the text.

and can be electronically calibrated for, a wide dynamic range. Pulses can be reconstructed with a precision which exceeds the intrinsic energy resolution of the calorimeters. The FEBs have excellent timing resolution for large pulses, less than the 70 ps result which can be measured due to jitter in pulses injected by the calibration board, so the final timing resolution will have to be extracted with beam particles. The coherent noise per channel is very low, typically 2–3% of the total noise. The calculations of the DSP on the RODs have been optimised and validated. The processing time of the DSP meets the specification for the maximum rate of L1 triggers. The stability of the electronics response is excellent, with only very small variations seen over a period of six months of operation.

Acknowledgments

We are greatly indebted to all CERN's departments and to the LHC project for their immense efforts not only in building the LHC, but also for their direct contributions to the construction and installation of the ATLAS detector, in particular the liquid argon calorimeter, and its infrastructure. We acknowledge equally warmly all our technical colleagues in the collaborating institutions without whom the liquid argon calorimeter could not have been built. A. Akimov, A. Hoffman, A. Lazarev, M. Mathieu, K. Sexton, and S. Shilov were especially instrumental in the installation of the detectors. Furthermore we are grateful to all the funding agencies which supported generously the construction and the commissioning of the liquid argon calorimeter and also provided the computing infrastructure. We acknowledge the support of NSERC, NRC and CFI, Canada; CERN; NSFC, China; IN2P3-CNRS and CEA-DSM, France; Bundesministerium fur Bildung,

2010 JINST 5 P09003

Wissenschaft, Forschung Technologie under contracts including number 05HA8EX16 (Wuppertal), Germany; INFN, Italy; CNRST, Morocco; Ministry of Education and Science and Innovations, and Russian Federal Agency of Atomic Energy; JINR; Slovak Grant Agency of the Ministry of Education of the Slovak Republic and the Slovak Academy of Sciences, Project No. 2/0061/08; Ministerio de Educación y Ciencia, Spain; The Swedish Research Council, The Knut and Alice Wallenberg Foundation, Sweden; Swiss National Science Foundation, and Canton of Bern and Geneva, Switzerland; National Science Council, Taiwan; Department of Energy and National Science Foundation, United States of America.

References

[1] ATLAS collaboration, G. Aad et al., *The ATLAS Experiment at the CERN Large Hadron Collider*, 2008 *JINST* **3** S08003.

[2] L. Evans and P. Bryant (eds.), *LHC Machine*, 2008 *JINST* **3** S08001.

[3] ATLAS collaboration, G. Aad et al., *Readiness of the ATLAS Liquid Argon Calorimeter for LHC Collisions*, arXiv:0912.2642, accepted for publication by Eur. Phys. J C.

[4] N.J. Buchanan et al., *ATLAS liquid argon calorimeter front end electronics*, 2008 *JINST* **3** P09003.

[5] LIQUID ARGON BACK END ELECTRONICS collaboration, A. Bazan et al., *ATLAS liquid argon calorimeter back end electronics*, 2007 *JINST* **2** P06002.

[6] N.J. Buchanan et al., *Design and implementation of the Front End Board for the readout of the ATLAS liquid argon calorimeters*, 2008 *JINST* **3** P03004.

[7] J. Colas et al., *Electronics calibration board for the ATLAS liquid argon calorimeters*, *Nucl. Instrum. Meth.* **A 593** (2008) 269.

[8] N.J. Buchanan et al., *Radiation qualification of the front-end electronics for the readout of the ATLAS liquid argon calorimeters*, 2008 *JINST* **3** P10005.

[9] J. Ban et al., *Radiation hardness tests of GaAs amplifiers operated in liquid argon in the ATLAS calorimeter*, *Nucl. Instrum. Meth.* **A 594** (2008) 389.

[10] C. Boulahouache et al., *The ATLAS LAr calorimeter Level 1 trigger signal pre-processing system: Installation, commissioning and calibration results*, accepted for publication in IEEE Trans. Nucl. Sci.

[11] J. Ban et al., *Cold electronics for the liquid argon hadronic end-cap calorimeter of ATLAS*, *Nucl. Instrum. Meth.* **A 556** (2006) 158;
E. Ladygin et al., *Preshaper for the hadronic endcap calorimeter*, available at https://edms.cern.ch/document/875444/1.

[12] W.E. Cleland and E.G. Stern, *Signal processing considerations for liquid ionization calorimeters in a high rate environment*, *Nucl. Instrum. Meth.* **A 338** (1994) 467.

[13] M. Aleksa et al., *ATLAS combined testbeam: computation and validation of the electronic calibration constants for the electromagnetic calorimeter*, ATL-LARG-PUB-2006-003,available at http://cdsweb.cern.ch/record/942528.

[14] D. Banfi, M. Delmastro and M. Fanti, *Cell response equalisation of the ATLAS electromagnetic calorimeter without the direct knowledge of the ionisation signals*, 2006 *JINST* **1** P08001.

2010 JINST 5 P09003

[15] C. Collard et al., *Prediction of signal amplitude and shape for the ATLAS electromagnetic calorimeter*, ATL-LARG-PUB-2007-010, available at http://cdsweb.cern.ch/record/1058294.

[16] ATLAS collaboration, G. Aad et al., *Drift Time Measurement in the ATLAS Liquid Argon Electromagnetic Calorimeter using Cosmic Muons*, arXiv:1002.4189.

[17] B. Chase et al., *Characterization of the coherent noise, electromagnetic compatibility and electromagnetic interference of the ATLAS EM calorimeter front end board*, in *Proceedings of the 5th Workshop on Electronics for the LHC Experiments (LEB 99)*, Snowmass, U.S.A., September 1999, pg. 222-226.

[18] G. Blanchot et al., *Electromagnetic compatibility of a DC power distribution system for the ATLAS liquid argon calorimeter*, in *Proceedings of the 11th Workshop on Electronics for LHC and Future Experiments (LECC 2005)*, Heidelberg, Germany, September 2005.

[19] ATLAS ELECTROMAGNETIC BARREL CALORIMETER collaboration, M. Aharrouche et al., *Energy linearity and resolution of the ATLAS electromagnetic barrel calorimeter in an electron test- beam*, *Nucl. Instrum. Meth.* **A 568** (2006) 601.

[20] ATLAS collaboration, *ATLAS detector and physics performance technical design report*, CERN-LHCC-99-014/015 (1999), available at http://atlasinfo.cern.ch/Atlas/GROUPS/PHYSICS/TDR/access.html.

[21] M. Aharrouche et al., *Time resolution of the ATLAS barrel liquid argon electromagnetic calorimeter*, *Nucl. Instrum. Meth.* **A 597** (2008) 178.

[22] J. Christiansen, A. Marchioro, P. Moreira and A. Sancho, *Receiver ASIC for timing, trigger and control distribution in LHC experiments*, *IEEE Trans. Nucl. Sci.* **43** (1996) 1773.

[23] Data sheet for the quartz crystal phase-locked loop (QPLL), available at http://proj-qpll.web.cern.ch/proj-qpll/.

2010 JINST 5 P09003